Two-step implantation of gold into graphene

Trentino, Alberto

2022-04-01

Trentino , A , Mizohata , K , Zagler , G , Laengle , M , Mustonen , K , Susi , T , Kotakoski , J & Ahlgren , E H 2022 , ' Two-step implantation of gold into graphene ' , 2D Materials , vol. 9 , no. 2 , 025011 . https://doi.org/10.1088/2053-1583/ac4e9c

http://hdl.handle.net/10138/353900
https://doi.org/10.1088/2053-1583/ac4e9c

Two-step implantation of gold into graphene

2D Materials

PAPER

Two-step implantation of gold into graphene

Alberto Trentino[1], Kenichiro Mizohata[2], Georg Zagler[1], Manuel Längle[1], Kimmo Mustonen[1], Toma Susi[1], Jani Kotakoski[1,*] and E Harriet Åhlgren[1,*]

[1] Faculty of Physics, University of Vienna, 1090 Vienna, Austria
[2] Faculty of Physics, University of Helsinki, PO Box 43, 00014 Helsinki, Finland
[*] Authors to whom any correspondence should be addressed.

E-mail: jani.kotakoski@univie.ac.at **and** harriet.ahlgren@univie.ac.at

Keywords: graphene, ion implantation, doping, gold, electron microscopy

OPEN ACCESS

RECEIVED
5 December 2021

REVISED
8 January 2022

ACCEPTED FOR PUBLICATION
24 January 2022

PUBLISHED
9 February 2022

Abstract

As a one-atom thick, mechanically strong, and chemically stable material with unique electronic properties, graphene can serve as the basis for a large number of applications. One way to tailor its properties is the controlled introduction of covalently bound heteroatoms into the lattice. In this study, we demonstrate efficient implantation of individual gold atoms into graphene up to a concentration of 1.7×10^{11} atoms cm^{-2} via a two-step low-energy ion implantation technique that overcomes the limitation posed by momentum conservation on the mass of the implanted species. Atomic resolution scanning transmission electron microscopy imaging and electron energy-loss spectroscopy reveal gold atoms occupying double vacancy sites in the graphene lattice. The covalently bound gold atoms can sustain intense electron irradiation at 60 kV during the microscopy experiments. At best, only limited indication of plasmonic enhancement is observed. The method demonstrated here can be used to introduce a controlled concentration of gold atoms into graphene, and should also work for other heavier elements with similar electronic structure.

1. Introduction

Introducing heteroatoms into graphene shows immense promise in manipulating the material's properties. B and N doped graphene for instance has been extensively studied for its performance in water splitting, oxygen reduction reaction, gas adsorption and supercapacitors [1]. Substitutional dopants from the transition metals group have been studied for their role in functionalizing graphene for single atom catalysis [2–4], surface adsorption for molecular sensing and trapping [5], and for tailoring graphene's electronic properties, magnetic moment and quantum topology [6–13].

Low-energy ion implantation offers an accurate and controllable way of introducing dopants into pristine structures without contamination from wet chemistry. It presents a scalable method for device fabrication, and due to the resulting covalently bonded structures, the dopant sites can be expected to remain unchanged over extended periods of time. B and N substitutions were the first successfully established dopants in graphene using low-energy ion implantation [14, 15]. Since then the method has been applied to introduce various dopant species in graphene: in addition to B and N [16–18], also P [19], Ge [20], and most recently Mn [21].

Direct ion implantation into graphene works efficiently when the momentum transfer from the projectile to the target atom is sufficient to knock out a carbon atom, and simultaneously allows the projectile itself to come to a halt at the vacated lattice site. Conversely, insufficient stopping becomes an issue when projectiles much heavier than carbon are considered. The displacement threshold energy of carbon in graphene is 21.14 eV [22]. This describes the minimum energy required to knock out a carbon atom in a pristine lattice. Assuming an elastic collision where momentum is conserved and C is at rest, an Au atom will retain over 88% of its initial velocity after the impact with C. The energy window to kick out the C and halt the ion at a created vacancy site thus becomes negligible. Nevertheless, since heavier atoms offer intriguing possibilities for property tailoring of graphene, overcoming poor implantation efficiency presents a major obstacle in functionalizing graphene for scalable applications. Gold is particularly interesting, because graphene-Au interfaces show tunable

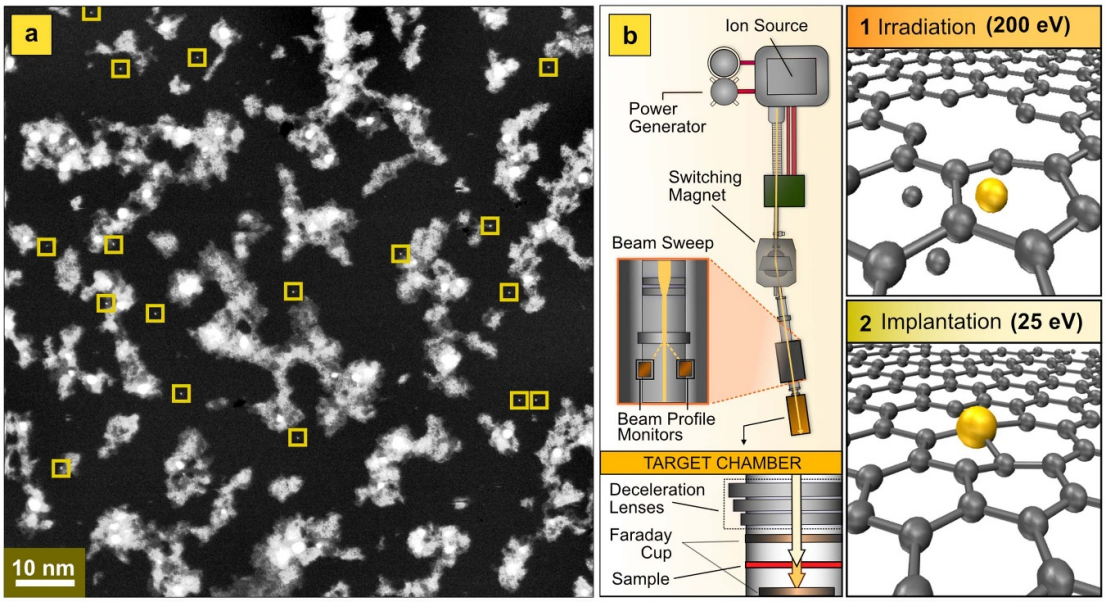

Figure 1. (a) A Gaussian-filtered MAADF STEM image of 125 × 125 nm^2 area of graphene after implantation with 200 and 25 eV Au. The dopants are clearly visible as bright points in the lattice, encircled with yellow squares for convenience. (b) A schematic displaying the ion beam line used for the implantation. The two-step implantation method is shown schematically in the insets marked 1 and 2 at the right side of the panel. Vacancies are first created by 200 eV Au irradiation directly followed by implantation at 25 eV [42].

localized surface plasmon resonances for plasmon-enhanced applications [23, 24] whilst single B, N and Si dopants in graphene have been associated with highly localized enhancement of graphene interband plasmon response [25, 26]. Au dopants in graphene could also open new routes for graphene spintronics, optoelectronics and single atom catalysis on two-dimensional surfaces [2, 6, 9].

Here we study the doping of graphene with single substitutional Au atoms. Since Au ($Z = 79$) is much heavier than carbon ($Z = 6$), we need to overcome the limitation imposed by momentum conservation. We do this using a combination of two implantation energies. The first irradiation with 200 eV Au creates lattice vacancies via the knock-on process, which is followed by soft landing of Au with 25 eV that leads into covalently bound substitutions through thermal diffusion and vacancy recombination. Complementary density functional theory calculations are employed to determine the energetics of the structures and image simulations to provide a comparison to experimental images. The created structure is further studied by electron energy-loss spectroscopy (EELS).

2. Results and discussion

The Au substitutions are easily found in STEM images due to the high contrast of the Au atom compared to graphene. An overview of 125×125 nm^2 area of the sample surface is shown in figure 1(a) with the Au substitutions encircled. The sample has a high quantity of single Au substitutions after the implantation over the entire sample surface.

The implanted concentration is estimated at about 1.7×10^{11} atoms cm^{-2} (compared to the irradiation dose of 10^{14} ions cm^{-2} which was same for both ion irradiation steps). The concentration is estimated by counting all the stable single implanted Au atoms within a representative sample area of 200×200 nm^2. The efficiency therefore represents both the ability of creating suitable vacancies as well as those vacancies to capture individual gold atoms to create a stable structure.

We note that additional gold atoms may be under the amorphous carbon contamination visible as white cloudy areas in figure 1(a). Also, any contaminants that are mobile on the sample surface, including Si atoms that are commonly found in graphene, may recombine with the created vacancies before the Au atoms are introduced and therefore reduce the reported efficiency. Also, any gold atoms landing on top of the contamination contribute to mobile structures that are for the most part unstable under the electron beam.

Surface contamination is common on all surfaces, and particularly visible on 2D samples. It is introduced during sample preparation and adsorbs directly from chemicals and/or air [27, 28]. Although steps were taken to reduce contamination in the samples before the implantation (see section 4), the samples were transported in ambient conditions

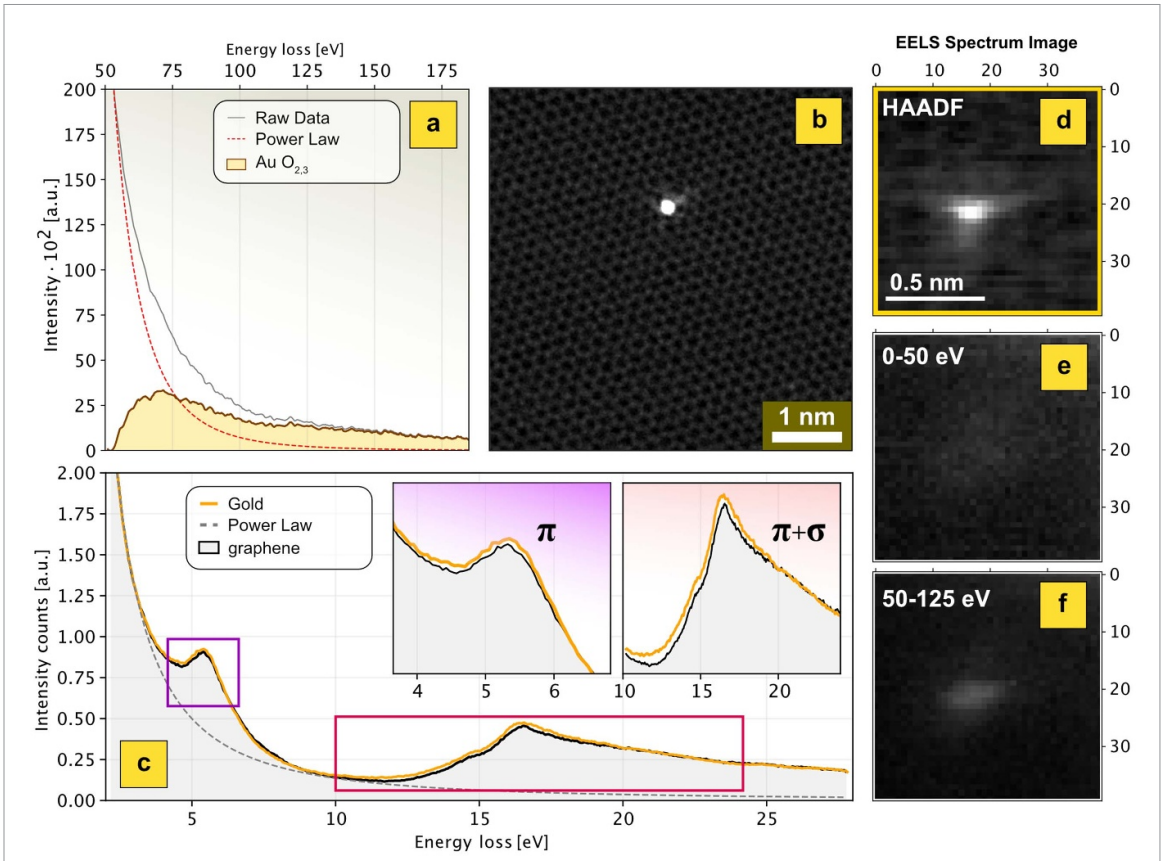

Figure 2. (a) Electron energy-loss spectrum of the Au $O_{2,3}$ edge. The background has been subtracted from the raw data (grey) using a power-law function (dashed red line). The filtered signal is showed in yellow. (b) STEM MAADF image of an implanted Au atom. (c) Plasmon π and $\pi+\sigma$ peaks of graphene (black) and the Au substitution site (yellow). The graphene and Au site were located more than 5 nm apart without contamination nearby (12 nm from visible contamination). (d)–(f) EEL spectrum images of graphene. From the top, 45×45 pixels STEM HAADF image corresponding to the spectrum maps below displaying graphene and the target Au atom by filtering over the relevant energy ranges: from 0–50 eV to 50–125 eV [42].

before and after the implantation leading to some amount of additional contamination.

The two-step implantation process combining the 200 and 25 eV energies is schematically illustrated in figure 1(b). The figure also displays the schematic of the implantation beam line KIIA and indicates the deceleration lens that is used to slow the energetic ions down to few tens of eV for the implantation. The Au dopants are found to be stable under 60 kV electron beam over long periods of imaging. A fourfold Au substituting two C atoms in graphene is shown in figure 2(b) with the surrounding graphene lattice clearly visible. All of the studied configurations show fourfold bonding into a graphene double vacancy under close inspection. However, the distinct brightness of the dopant in HAADF and MAADF makes it challenging to see the local bonding around the Au atom. Thus, we compare the location of the maximum intensity of the dopant to the surrounding pristine lattice in order to extract the location of the Au in respect to the graphene lattice, as shown later. Additionally, due to the brightness of the Au, remaining aberrations in the objective lens can manifest as a halo around the point of maximum intensity, which is seen in some of the images.

The 200 eV Au irradiation during step one is expected to create mainly of mono- and divacancies. It is likely that not all of them are filled during the second step. While the remaining vacancies can also be healed through annealing-treatment [29], any that still remain may affect the properties of graphene [30]. The performance of the altered structures will depend on the application and should be carefully considered.

EELS measured at the dopant site confirms the chemical identity of the heteroatom. The energy-loss region presented in figure 2(a) shows a signal starting at 60 eV energy-loss measured from a single dopant. Localization of the Au $O_{2,3}$ edge was further confirmed through the acquisition of a 45×45 pixels EELS map filtered in the energy-loss range between 50 and 125 eV (figure 2(d–f)). We also measure the low-loss range of the EELS spectrum characteristic for graphene interband plasmon resonance peaks that arise from the collective oscillations of π and $\pi+\sigma$ valence electrons [31] located at 4.7 and 14.6 eV energy loss. Although apparent changes in

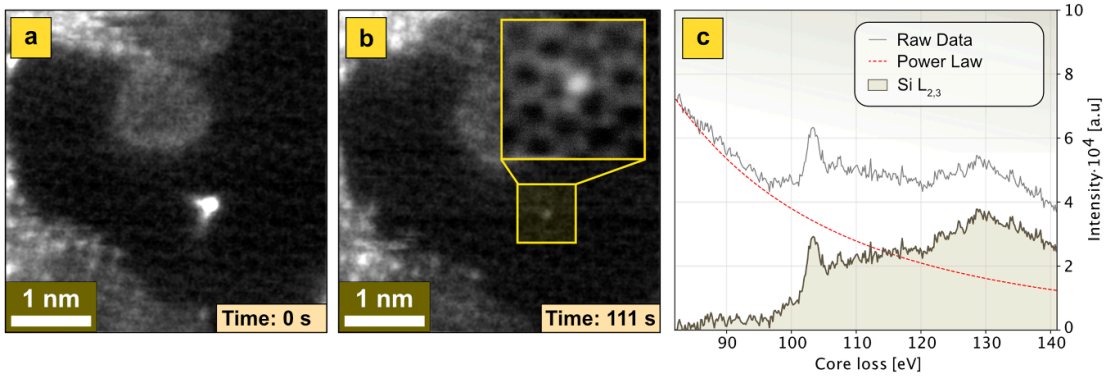

Figure 3. ((a), (b)) Two STEM MAADF images showing the instability of the apparent three-coordinated Au atom found after lasering. (a) A gold atom is visible in clean graphene. (b) After a few scans, the gold atom disappears revealing a silicon atom at the same location. (c) EELS core-loss confirming the identity of the Si atom in panel (b) [42].

the plasmon peaks at the dopant site can be seen (figure 2(c)), due to instrumental broadening of the zero-loss-peak, it is impossible to make a conclusive even qualitative statement about the effect for the quality factors of the plasmon peaks. Thus, we conclude that the Au dopant in a double vacancy site in graphene has a negligible effect in the interband plasmon resonance of the material.

The sample was further annealed in the microscope column with a 100 ms laser pulse at 60 mW to provide large clean areas [32]. This treatment triggers the thermal activation and diffusion of inherent Si adatom impurities that are commonly found in graphene [33], as well as any Au adatoms loosely bound on contaminated regions after the implantation. Thermal activation of adatom diffusion is a viable method to include impurities in vacancy-type defects in carbon nanomaterials. The diffusing Si can become trapped in point vacancies and provide metastable sites for any other diffusing species. Such individual Si impurities anchoring atoms on graphene was recently reported for small In clusters [34]. In other experiments, diffusing Si atoms have been observed to replace P and Ge impurity atoms during observation [19, 20]. In our Au-implanted samples we observe some apparently 3-coordinated Au atoms only after laser cleaning, and they all turn into Si impurities during observation (figure 3). Due to the high scattering intensity and the poor beam-stability of these structures, our experimental evidence does not allow differentiating between Au captured at Si impurity sites and the dynamic replacement process.

2.1. Theoretical considerations

To further investigate the Au dopant and its stability we performed density functional theory based structural optimization on the observed Au in fourfold (Au@C4) and the apparent threefold (Au@C3) configurations, see table 1. The Au binding energy for Au@C4 is as much as 2.9 eV lower than that of the Au@C3. The Au@C4 is closer to a planar structure, with the Au elevated by 0.70 Å from the lattice plane, whereas in Au@C3, it is pushed out of the lattice plane by as much as 1.99 Å. Our results are in line with previous theoretical work [35]. The lower stability of the Au@C3 can explain why hardly any such configurations were detected during imaging before laser cleaning. Another likely reason for this is that the impinging Au is more likely to displace two carbon atoms rather than a single one during the impact due to the large mass ratio of 16:1 between the atoms. In addition, we calculated the binding energy of an Au adatom to be −0.51 eV at the expected top adsorption site [36]. Based on this relatively low energy, we expect Au adatoms to be highly mobile at room temperature, diffusing along the carbon-carbon bridge sites as shown previously [36].

Table 1. Optimised configurations of Au in fourfold (Au@C4) and threefold (Au@C3) sites in graphene, as well as an adatom far away from the double vacancy (adAu). The binding energy E_B (energy difference of the relaxed structures with respect to the same structure where the Au atom is placed far away in vacuum), the Au-C distance d and the elevation of the Au from the graphene lattice plane Δh in the optimized structure are given.

Site	E_B (eV)	d (Å)	Δh (Å)
Au@C4	−5.00	2.00	0.70
Au@C3	−2.10	2.07	1.99
adAu	−0.51	2.33	2.53

Image simulations are shown alongside the optimized structures in figures 4(a) and (b). The calculated Bader charges [37] do not show significant difference in the electron exchange between Au and the neighboring C in each structure, 0.127 e^- per C for Au@C4 and 0.134 e^- per C for Au@C3.

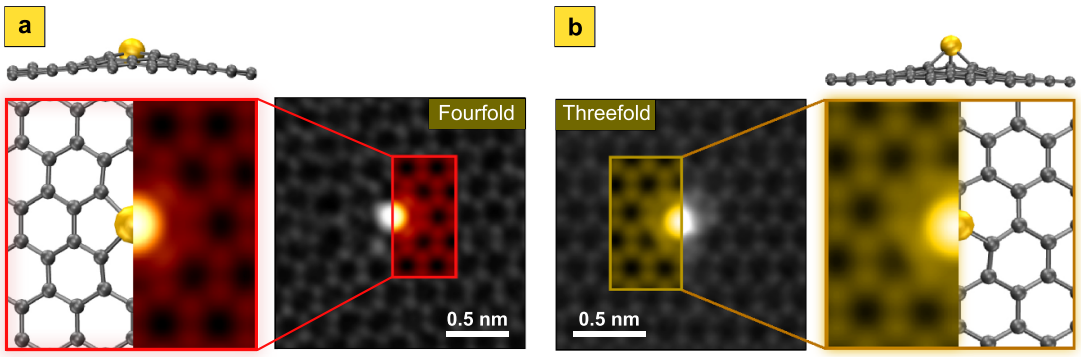

Figure 4. (a) Four- and (b) threefold Au@C4 and Au@C3 structures. The top and side view of the optimized structures from density functional theory calculations are shown with the ball-and-stick visualization at the left and right edges. The corresponding image simulations are shown for both structures in red and yellow color schemes, respectively. MAADF STEM images of a Au@C4 and an apparent Au@C3 structure are shown in grayscale with simulated images overlaid for comparison. Note that all apparent Au@C3 were observed after laser cleaning and converted into individual Si impurity sites during observation [42].

3. Conclusions

We present an effective method for incorporating single Au dopants into substitutional sites in graphene by combining two implantation energies. This can be used to introduce a controlled and rather high concentration of Au into graphene. The technique overcomes the conventional limitation arising from the insufficient stopping of the heavy dopant by the much lighter target atom and should be applicable for other heavier elements with a similar electronic structure. The covalently bound Au atoms are stable over long times and even under the electron beam, indicating promise for applications in single atom catalysis on two dimensional surfaces. These single Au dopants in graphene could open new routes for graphene spintronic, optoelectronics and catalysis applications.

4. Methods

The commercially purchased monolayer graphene samples on Quantifoil Au TEM grids from Graphenea were heated for 1 h at 140 °C to reduce contamination before low-energy ion implantation was conducted with the 500 kV KIIA ion implanter at the University of Helsinki. In the setup, the ions are extracted at 30 kV and 10 mA. The beam is mass-filtered with a with a double-focusing 90 ° analyzing magnet creating an isotopically pure beam of positive ions. The ion beam is then accelerated over the main high voltage potential (0–470 kV) in the accelerating tube, focused by electrostatic quadrupole triplet lenses, and steered by a switching magnet through the implantation beam line. A neutral trap is included to remove neutral particles. The trap consists of horizontal deflection plates connected to a DC voltage bending the beamline a few degrees. The charged particles will follow the bend in the beamline while neutral particles continue in straight line and do not reach the target chamber where the final deceleration takes place in a deceleration lens. The lens consists of three cylindrical elements, creating a decelerating electric field for the charged ions. The implantation fluence is monitored by scanning over four off-axis Faraday cups located outside of the target area.

The electrostatic deceleration lens was fitted to the beam line to allow implantation at ultra-low energies. The beam was swept over the area of 1 cm^2 ensuring irradiation of the entire sample surface. The samples were first irradiated with 200 eV Au with the dose 10^{14} ions cm^{-2}, immediately followed by implantation at 25 eV with the same dose. The energy of the ions at the very low energy range is a distribution centered at the chosen energy with a small tail extending to higher energies. Therefore, we can not completely exclude energy contamination from ions with slightly higher energy than the intended.

After the implantation the samples were characterized with an aberration-corrected Nion UltraSTEM100 scanning transmission electron microscope (STEM) at the University of Vienna operated at 60 kV acceleration voltage. The angular range of the HAADF and MAADF detectors were 80–300 mrad and 60–200 mrad, respectively, and the convergence semiangle was ca. 30 mrad. EEL spectra were recorded with a Gatan PEELS 666 spectrometer with an Andor iXon 897 electron-multiplying charge-coupled device (EMCCD) camera. The energy dispersion was 0.3 eV/pixel.

To model the Au substitutions, we replaced either one or two C atoms in a 7×7 orthorhombic supercell of graphene (97 or 98 atoms in total), and relaxed its structure using density functional theory (DFT) with the GPAW package. We used a plane-wave basis set with a cutoff energy of 600 eV and 3×3×1 Monkhorst–Pack **k**-points to sample the Brillouin zone, and optimized both the cell and

atomic positions using the PBE functional [38] to describe exchange and correlation. Binding energies of Au atoms into single and double vacancies and as adatoms were estimated by comparing the total energies of systems with the Au atom either placed far away in vacuum, bonded into the vacancy, or as an adatom far away from the vacancy. To obtain comparable realistic energies for the Au adatoms [36], we re-optimized all atomic positions with the C09 van der Waals functional [39].

The DFT-relaxed structures of a single Au atom bonded to either the single or double vacancy were used as input for image simulations using the multislice algorithm as implemented in the abTEM code [40]. For the scattering potential, we tested both the full electrostatic potential derived from the DFT electron density as well as the independent atom model as parametrized by Lobato and Van Dyck [41], and found only negligible differences in the resulting annular dark field scattering intensities. We used a real-space sampling of 0.04 Å for the potential and a slice thickness of 0.1 Å. The scan area covered 6×10 Å^2 centered on the Au impurity with slightly better than Nyquist sampling, and intensity line profiles interpolated. The probe and detector parameters were set to match the experiment. Neither partial coherence nor thermal diffuse scattering was included in the simulations.

Data availability statement

The data that support the findings of this study are openly available at the following URL/DOI: http://phaidra.univie.ac.at/o:1400827.

Acknowledgments

A T, M L and J K acknowledge funding from Austrian Science Fund (FWF) through project P31605-N36 and E H Å through Project No. M2595. T S received funding from the European Research Council (ERC) under the European Union's Horizon 2020 research and innovation programme (Grant Agreement No. 756277-ATMEN). Computational resources from the Vienna Scientific Cluster (VSC) are gratefully acknowledged.

ORCID iDs

Alberto Trentino https://orcid.org/0000-0003-0229-3313
Kenichiro Mizohata https://orcid.org/0000-0003-1703-2247
Georg Zagler https://orcid.org/0000-0002-2355-6189
Manuel Längle https://orcid.org/0000-0002-4126-4059
Kimmo Mustonen https://orcid.org/0000-0002-0953-7299
Toma Susi https://orcid.org/0000-0003-2513-573X
Jani Kotakoski https://orcid.org/0000-0002-1301-5266
E Harriet Åhlgren https://orcid.org/0000-0002-3876-8547

References

[1] Rao C N R, Gopalakrishnan K and Govindaraj A 2014 *Nano Today* **9** 324–43
[2] Deng D, Novoselov K S, Fu Q, Zheng N, Tian Z and Bao X 2016 *Nat. Nanotechnol.* **11** 218–30
[3] Lu Y H, Zhou M, Zhang C and Feng Y P 2009 *J. Phys. Chem.* C **113** 20156–60
[4] Ta H Q *et al* 2018 *Nano Res.* **11** 2405–11
[5] Cortés-Arriagada D, Villegas-Escobar N and Ortega D E 2018 *Appl. Surf.* **427** 227–36
[6] Krasheninnikov A V, Lehtinen P O, Foster A S, Pyykkö P and Nieminen R M 2009 *Phys. Rev. Lett.* **102** 126807
[7] Åhlgren E H, Markevich A and Besley E 2018 *J. Phys. Chem.* C **122** 25700–8
[8] Robertson A W *et al* 2013 *Nano Lett.* **13** 1468–75
[9] Santos E J G, Ayuela A and Sánchez-Portal D 2010 *New J. Phys.* **12** 053012
[10] Tang Y, Yang Z and Dai X 2011 *J. Chem. Phys.* **135** 224704
[11] Dyck O *et al* 2021 *Carbon* **173** 205–14
[12] Thakur J, Saini H S, Singh M, Reshak A H and Kashyap M K 2016 *Physica* E **78** 35–40
[13] Zan R, Bangert U, Ramasse Q and Novoselov K S 2011 *Nano Lett.* **11** 1087–92
[14] Åhlgren E H, Kotakoski J and Krasheninnikov A V 2011 *Phys. Rev.* B **83** 115424
[15] Bangert U *et al* 2013 *Nano Lett.* **13** 4902–7
[16] Kepaptsoglou D *et al* 2015 *ACS Nano* **9** 11398–407
[17] Bangert U *et al* 2017 *Ultramicroscopy* **176** 31–6
[18] Cress C D, Schmucker S W, Friedman A L, Dev P, Culbertson J C, Lyding J W and Robinson J T 2016 *ACS Nano* **10** 3714–22
[19] Susi T *et al* 2017 *2D Mater.* **4** 021013
[20] Tripathi M, Markevich A, Böttger R, Facsko S, Besley E, Kotakoski J and Susi T 2018 *ACS Nano* **12** 4641–7
[21] Lin P C *et al* 2021 *ACS Nano* **15** 5449–58
[22] Susi T, Hofer C, Argentero G, Leuthner G T, Pennycook T J, Mangler C, Meyer J C and Kotakoski J 2016 *Nat. Commun.* **7** 13040
[23] Li X, Zhu J and Wei B 2016 *Chem. Soc. Rev.* **45** 3145
[24] Iyer G R S, Wang J, Wells G, Guruvenket S, Payne S, Bradley M and Borondics F 2014 *ACS Nano* **8** 6353–62
[25] Hage F S *et al* 2018 *ACS Nano* **12** 1837–48
[26] Zhou W, Lee J, Nanda J, Pantelides S T, Pennycook S J and Idrobo J C 2012 *Nat. Nanotechnol.* **7** 161–5
[27] Peng Z, Yang R, Kim M A, Li L and Liu H 2017 *RSC Adv.* **7** 27048–57
[28] Algara-Siller G, Lehtinen O, Turchanin A and Kaiser U 2014 *Appl. Phys. Lett.* **104** 153115
[29] Chen J, Shi T, Cai T, Xu T, Sun L, Wu X and Yu D 2013 *Appl. Phys. Lett.* **102** 103107
[30] Banhart F, Kotakoski J and Krasheninnikov A V 2011 *ACS Nano* **5** 26–41
[31] Eberlein T, Bangert U, Nair R R, Jones R, Gass M, Bleloch A L, Novoselov K S, Geim A and Briddon P R 2008 *Phys. Rev.* B **77** 233406
[32] Trentino A, Madsen J, Mittelberger A, Mangler C, Susi T, Mustonen K and Kotakoski J 2021 *Nano Lett.* **21** 5179–85
[33] Inani H *et al* 2019 *J. Phys. Chem.* C **123** 13136–40

[34] Elibol K et al 2021 ACS Nano 15 14373–83
[35] Malola S, Häkkinen H and Koskinen P 2009 Appl. Phys. Lett. 94 043106
[36] Amft M, Lebègue S, Eriksson O and Skorodumova N V 2011 J. Phys. Condens. Matter 23 395001
[37] Bader R F W 1985 Acc. Chem. Res. 18 9–15
[38] Perdew J P, Burke K and Ernzerhof M 1996 Phys. Rev. Lett. 77 3865–8
[39] Cooper V R 2010 Phys. Rev. B 81 161104
[40] Madsen J and Susi T 2021 Open Res. Eur. 1 13015
[41] Lobato I and Van Dyck D 2014 Acta Crystallogr. 70 636–49
[42] Harriet Åhlgren E 2021 Original data related to manuscript 'Two-step implantation of gold into graphene', Phaidra (available at: https://phaidra.univie.ac.at/view/o:1400827)